Bonding between silicones and thermoplastics using 3D printed mechanical interlocking

Rossing, Lars; Scharff, Rob B.N.; Chömpff, Bryan; Wang, Charlie C.L.; Doubrovski, Eugeni L.

DOI
10.1016/j.matdes.2019.108254

Publication date
2020

Document Version
Final published version

Published in
Materials and Design

Citation (APA)
Rossing, L., Scharff, R. B. N., Chömpff, B., Wang, C. C. L., & Doubrovski, E. L. (2020). Bonding between silicones and thermoplastics using 3D printed mechanical interlocking. *Materials and Design*, *186*, Article 108254. https://doi.org/10.1016/j.matdes.2019.108254

Materials and Design 186 (2020) 108254

Contents lists available at ScienceDirect

Materials and Design

journal homepage: www.elsevier.com/locate/matdes

Bonding between silicones and thermoplastics using 3D printed mechanical interlocking

Lars Rossing [a,**], Rob B.N. Scharff [b], Bryan Chömpff [c], Charlie C.L. Wang [d], Eugeni L. Doubrovski [b,*]

[a] Ultimaker B.V., Geldermalsen, the Netherlands
[b] Industrial Design Engineering, Delft University of Technology, Delft, the Netherlands
[c] Zuyd University of Applied Sciences, Heerlen, the Netherlands
[d] Department of Mechanical and Automation Engineering, The Chinese University of Hong Kong, Shatin, Hong Kong

HIGHLIGHTS

- New 3D printed structures create a strong bonding between silicone and plastic.
- Hybrid fabrication is used to cast silicone onto a 3D-printed mold and structure.
- A verified model relates the bonding strength to the structure's parameters.
- A CAD tool generates the developed interlocking structure onto product interfaces.
- The bonding structure is applied in soft robots, sealings, and overmolded parts.

GRAPHICAL ABSTRACT

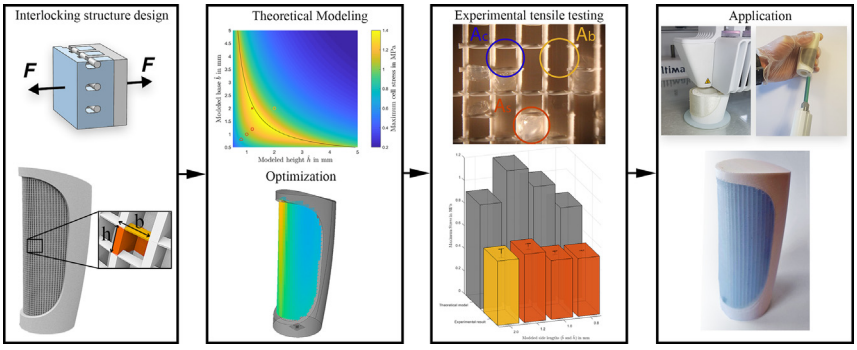

ARTICLE INFO

Article history:
Received 30 July 2019
Received in revised form 1 October 2019
Accepted 3 October 2019
Available online 11 October 2019

Keywords:
Silicones
3D printing
Mechanical interlocking
Fused Deposition Modeling
Casting
Bonding

ABSTRACT

Silicones have desirable properties such as skin-safety, high temperature-resistance, and flexibility. Many applications require the presence of a hard body connected to the silicone. Traditionally, it has been difficult to create strong bonding between silicones and hard materials. In this study, a technique is presented to control the bonding strength between silicones and thermoplastics through mechanical interlocking. This is realized through a hybrid fabrication method where silicone is cast onto a 3D-printed mold and interlocking structure. The influence of the structure's design parameters on the bonding strength is explored through theoretical modeling and physical testing, while the manufacturability of the 3D-printed structure is ensured. A CAD tool is developed to automatically apply the interlocking structure to product surfaces. The user interface visualizes the theoretical strength of the cells as the designer adjusts the cell parameters, allowing the designer to iteratively optimize the structure to the product's load case. The bonding strength of the presented mechanical interlocking structure is more than 5.5 times higher than can be achieved with a commercially available primer. The presented technique enables custom digital design and manufacturing of durable free-form parts. This is demonstrated through application of the technique in over-molded products, airtight seals, and soft pneumatic actuators.

* Corresponding author.
** Corresponding author.
E-mail addresses: l.rossing@ultimaker.com (L. Rossing), e.l.doubrovski@tudelft.nl (E.L. Doubrovski).

https://doi.org/10.1016/j.matdes.2019.108254

1. Introduction

Many products are composed of parts that are a combination of hard and soft materials. Kitchen utensils, toothbrushes, car parts, and integrated seals are common examples. This also includes products where the soft material is a silicone [1]. Silicones, or *Polydimethylsiloxanes*, are soft materials that have desirable properties for applications that require high flexibility, high temperature resistance, or skin-safety [2]. We aim to enable the use of 3D printing to fabricate parts with hard (thermoplastic) material and soft silicone. Compared to traditional manufacturing, 3D printing provides more freedom in fabricating complex geometry and custom parts. The ability to create complex geometries and custom parts with hard materials and silicones is relevant for various applications. One such an area is soft robotics [3], where silicones are a popular choice for the fabrication of soft actuators [4]. Another area where 3D printing this combination of materials could be useful is multi-material compliant mechanisms [5,6]. Here, silicone can be used as a soft member to transfer motion, force, and energy for specific applications. However, 3D printing silicones in combination with thermoplastics is not straightforward due to challenges in bonding between the two materials and 3D printing process incompatibility, as described below.

Good bonding between the hard and soft materials is essential for the functionality of the products. This is generally achieved by using compatible materials [7] which increases the physico-chemical adhesion phenomenon [8]. When the materials are incompatible or more bonding strength is required, mechanical interlocking using large features can be a solution [9]. Using 3D printing, large-scale features such as dog bones and hooks have been shown to improve the bonding between a soft and hard material [10]. Although a high bonding strength was achieved, the scale of the features poses significant limitations to the design of the parts. Condensation curing silicones, also known as one-component *Room Temperature Vulcanization* (RTV) silicones, have good adhesion to surfaces with hydroxyl groups thanks to their cross-linking mechanism [2]. Compared to condensation curing silicones, hydrosilylation curing silicones, have favorable properties, especially for soft robotics and medical applications. This is because hydrosilylation curing silicones produce no decomposition products during curing and the curing can be done in an enclosed volume. Also, they have limited shrinkage, better heat resistance, and are food safe. However, hydrosilylation silicones do not exhibit sufficient adhesion forces to any thermoplastic substrates for most applications [1,2]. Chemical bonding between silicones and thermoplastics can be somewhat improved by applying a primer or plasma treatment to the contact surface. Integrating a primer step into the printing process is not a preferred direction due to environmental and cost aspects [11]. Atmospheric Pressure Plasma Jets have been proposed in 3D printers [12] to increase inter layer adhesion, however wettability of the treated surface decreases over time [13] hence, casting the silicone after printing would result in graded adhesion strength. Furthermore, the adhesion strength of non adhesion modified silicone on plastic surfaces treated with this process might be too weak for demanding applications [1] as for example seen in the field of soft robotics. Therefore, to be able to 3D print reliable parts with these silicones, challenges with bonding the silicone to hard materials need to be addressed.

There are several *Additive Manufacturing* (AM) - or 3D printing - solutions that can fabricate silicone parts. 3D printing technologies that can process silicones have been developed in the AM categories Material Extrusion [14], Vat photopolymerization, and Material Jetting [15]. These printers can fabricate silicone parts, but without a secondary (hard) material. While *Multi-Material Additive Manufacturing* (MMAM) systems are used to combine hard and soft materials [16], the soft materials are not silicones, and therefore do not have the properties of silicones that make them appropriate for many of the discussed applications. The use of silicones in MMAM is not straightforward, not only due to poor bonding, but also because printing silicones generally requires a different AM process compared to printing the hard part. A solution is multi-process 3D printing, in which the AM process is enhanced with complementary processes to increase component functionality [17]. An example of this is the *Hybrid Deposition Manufacturing* (HDM) setup as proposed by Ma et al. [10] and Rossing [18]. These works demonstrate an approach where both a thermoplastic part and the mold for a resin part are printed using *Fused Deposition Modeling* (FDM), after which the mold is filled with a resin of soft (poly-)urethanes. The mold material can then be removed by breaking it or dissolving it in water (Fig. 1). This setup can be used for rapid prototyping of overmolded hard-soft parts, manufacturing low volume (custom) hard-soft parts and complex components that are difficult to make with traditional manufacturing processes [10]. The work of Rossing [18] demonstrates an integrated casting system which combines 3D printing with a low pressure casting step in one autonomous manufacturing process. These HDM setups could be used to manufacture 3D printed thermoplastic parts combined with cast silicones. However, this requires addressing the bonding issues discussed earlier.

Studies investigating bonding in MMAM differ in process, material, and testing methods. There is no standard for testing 3D printed multi-material interfaces [19]. The wide variety of tests that can be performed to investigate adhesion include tensile tests, fracture tests, and impact tests [20]. For example, Hudiakova et al. [21] use both double cantilever beam and cracked round bar tests to characterise interlayer cohesion between FDM printed polylactic acid (PLA) and short carbon fibre reinforced PLA. Vu et al. [22] use a variety of double cantilever beam test setups to characterise a multi-material 3D printed interface between a hard and soft material. With the same process and materials, Lumpe et al. [23] use geometries according to the ASTM D638-14 standard [24] to test interface strength for quasi-static loading. Specific test methods for 3D printed mechanical interlocking structures were not found.

Addressing the mentioned issues of the bonding and manufacturing process, we present a structure of 3D printed mechanical interlocking cells that locally increase the bonding strength between hard thermoplastics and silicones, without significantly impacting the design freedom and customizability. As the structure has a small depth and is guaranteed to be 3D printable in all directions, it can be automatically generated and applied to planar and curved contact surfaces. The influence of the structure's design parameters on the bonding strength is explored through theoretical modeling and physical testing. The unit cells are applied to a double curved multi-material bike handle, integrated seals, and a novel air-tight soft pneumatic actuator benefiting from the possibility to locally control the bonding between the two materials.

2. Method

2.1. Unit cell for mechanical interlocking

Because silicones are known to have minimal adhesion with thermoplastics, mechanical interlocking was chosen to facilitate the bonding. The proposed interlocking structure is composed of arrays of unit cells. The design of the unit cell is based on three considerations; bonding strength, manufacturing constraints, and applicability.

- **Bonding strength**: The volume of the thermoplastic interlocking structure locally reduces the volume fraction of the silicone. As a result, the area of the silicone at any cross section will be decreased with an increased feature size of the thermoplastic structure. A smaller total area of silicone in a cross section perpendicular to the loading direction leads to higher stresses in the silicone. Therefore, to maximize the strength of the silicone structure at the interface, the feature size of the thermoplastic structure should be minimized.
- **Manufacturing constraints**: Both the 3D printing and the casting processes were considered for the design of the unit cell. The printed structure should have a designed minimal feature size of 0.4 mm,

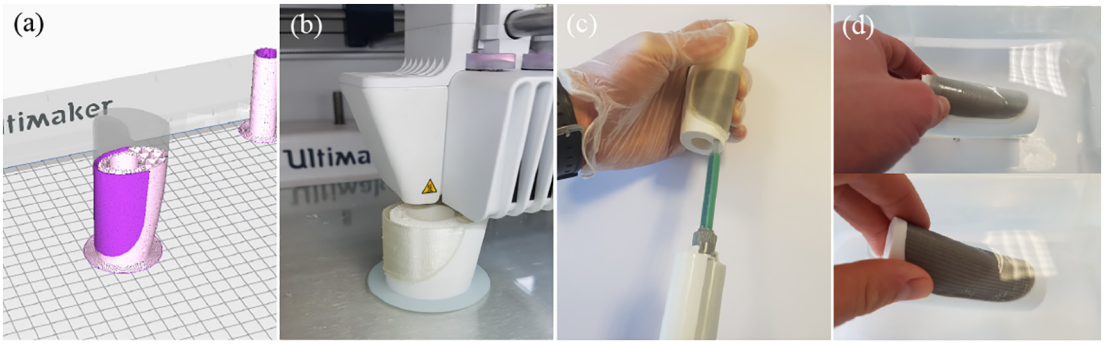

Fig. 1. Hybrid Deposition Manufacturing process used in this paper. (a) Slicing of part in printer software. Hard material is indicated in pink, sacrificial mold part is indicated in purple. (b) Printing of part with sacrificial mold. (c) Low pressure casting of silicone. (d) Curing and demolding.

which is the size of the used extrusion nozzle of the 3D printer. Discontinuities of the 3D printer's toolpath generally lead to loss in printed quality. Therefore, the structure must be designed to have slices with long continuous toolpaths with few discontinuities. To be able to 3D print overhangs properly, overhanging elements need to be designed to link two non-overhanging points in a straight line, so that the principle of bridging can be applied [25]. The individual cavities of each cell require vertical connectivity to allow air to escape during the casting of the silicone. The dimensions of these cavities cannot be made too small, as that could prevent their filling by the viscous silicone.

- **Applicability**: An important characteristic of the unit cell is its applicability to a large variety of products. Smaller features of the structure minimize the impact on the design of the product. The depth of the unit cell determines the minimal interface thickness, while the unit cell size determines the minimal feature size.

Arrays of cells create the interlocking structure, the CAD design of the structure is illustrated in Fig. 2(a). The structure is composed of vertical elements connected with horizontal crossover beams bridging between the vertical elements. When sliced by the 3D printer's software, the toolpaths for the vertical elements and for the horizontal crossover beams form a continuous extrusion within each layer. A visual representation of the printer's toolpaths is illustrated in Fig. 2(b). To evaluate the dimensions of the printed structure, a sample array was printed and 3D scanned. 3D scanning was done with a *GOM ATOS Core* scanner (0.032 mm measuring point distance). The 3D mesh that resulted from the scan is shown in Fig. 2(c). While the vertical beams were modeled to have a thickness of 0.4 mm in the CAD model, their average thickness was measured to be 0.5 mm. As expected, the horizontal crossover beam that was modeled to be rectangular, was found to have a more circular cross section once printed. The measured thickness of the horizontal beams was 0.4 mm. With the used slicing settings, the horizontal beams were printed by two extrusion passes, while one pass is sufficient. This resulted in a somewhat irregular shape of the horizontal beams, as can be seen in Fig. 2(c).

The silicone is cast onto the structure, encapsulating the crossover beams to create interlocking between the silicone and thermoplastic. A graphical illustration of this interlocking is shown in Fig. 3(a). When loaded, the crossover beams lock up the silicone that was cast into the structure, as illustrated in Fig. 3(b).

2.2. Modeling

A theoretical model was developed to better understand the relation between the structure's design parameters and its bonding strength. First, the scope was reduced to the smallest repetitive unit in the structure, which is illustrated in Fig. 3(c). Depending on the chosen dimensions of the design parameters, three different failure modes could be expected; failure of the plastic crossover beam, failure in the silicone surface A_s, and failure in the silicone at surface A_c. (see Fig. 3(d and e)).

The stress in a single cell σ_c can be calculated as:

$$\sigma_c = \frac{F_c}{A_s + A_b + A_r} = \frac{F_c}{b\,h} + 2\,r\,b + t\,(h + 2\,r) \tag{1}$$

As the crossover beams are encapsulated in the silicone and are relatively short, the beams are expected to fail mainly due to shear stress. This was later confirmed by the tensile test results shown in Fig. 7, that show a failure of the beams at the connections with the vertical elements, where the highest shear stress occurs. In contrast, failure due to bending stress would occur in the middle of the crossover beam. As discussed in section 2.1, the 3D printed beam is circular. The shear stress of a circular beam can be calculated as:

$$\tau_b = \frac{4\,V^2}{3\,c\,r} \tag{2}$$

where V indicates the shear force. As V is equal to $\frac{1}{2}F_c$ (see Fig. 3(f)), the

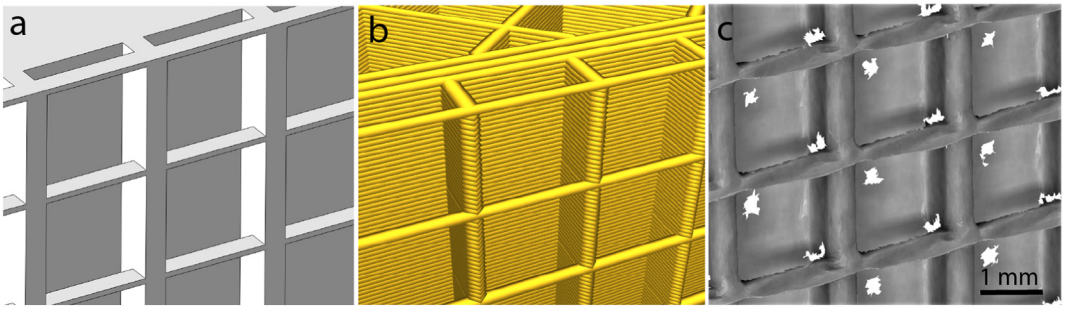

Fig. 2. (a) CAD model of cell array. (b) Visualization of toolpath created by printer's slicing software. (c) 3D scan of printed structure.

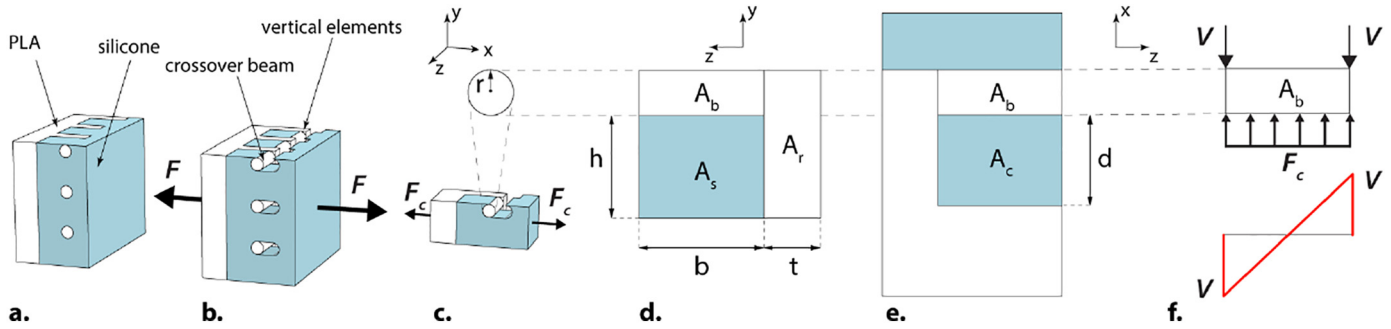

Fig. 3. Forces and parameters of the mechanical interlocking structure. (a) Unloaded mechanical interlocking surface. (b) Loaded mechanical interlocking surface. (c) Loaded mechanical interlocking cell. (d) Cell parameters at cross-section through the center of the crossover beam in the *yz*-plane. (e) Cell parameters at cross-section through the center of the crossover beam in the *xz*-plane. (f) Free body diagram and shear force diagram at cross-section through the center of the crossover beam in the *xz*-plane.

maximum cell force for the beam ($F_{c,b_{max}}$) can be calculated as:

$$F_{c,b_{max}} = \tau_{b_{yield}} \frac{3\,\pi\, r^2}{2} \tag{3}$$

where $\tau_{b_{yield}}$ is the shear yield strength of the crossover beam's material. The silicone surface A_s fails on tension. Thus, $F_{c,s_{max}}$ can be calculated as:

$$F_{c,s_{max}} = \sigma_{s_{yield}}\, A_s \tag{4}$$

Finally, the maximum cell force $F_{c_{max}}$ is given as the lowest of the two:

$$F_{c_{max}} = \min F_c, b_{max}, F_c, s_{max} \tag{5}$$

Radius r was set at 0.2 mm (i.e. the measured radius of the printed beam, as discussed in section 2.1). The yield strength of the PLA was determined at 49 MPa. According to the maximum shear stress theory, this results in a shear yield strength of (0.5∗49 = 24.5 MPa). The yield strength of the silicone $\sigma_{s_{yield}}$ was determined at 2.5 MPa. The CAD drawing of the crossover beams has a height of 0.1 mm. However, with the beam's measured diameter (and height) of 0.4 mm, the height h of surface A_s is reduced. Therefore, the real height h of the cell is converted to the modeled value $\hat{h}$ that would realize such a height: $h = \hat{h} - 0.3$. Similarly, the fabricated base b is converted to the modeled base $\hat{b}$ to correct for larger size of the printed vertical beams compared to the CAD design: $b = \hat{b} - 0.1$. For these values, Fig. 4 shows the maximum stress $\sigma_{c_{max}}$ (using the obtained $F_{c_{max}}$ in eq. (1)) as a function of the modeled parameters $\hat{b}$ and $\hat{h}$. The black line indicates the sample dimensions for which $F_{c,b_{max}} = F_{c,s_{max}}$. The highest achievable maximum cell stress can be found on this line. Samples on the left side of this line (indicated in red) are expected to fail on the silicone, whereas samples on the right side of the line (indicated in yellow) are expected to fail due to shear stress in the crossover beam.

This theoretical model is based on several assumptions. For instance, the model shown in Fig. 4 assumes that the failure does not occur at surface A_c. Moreover, the model ignores fabrication artefacts and inaccuracies, such as sagging of the beam, an inconsistent cross-section of the beam, and imperfect casting, which can significantly affect the strength

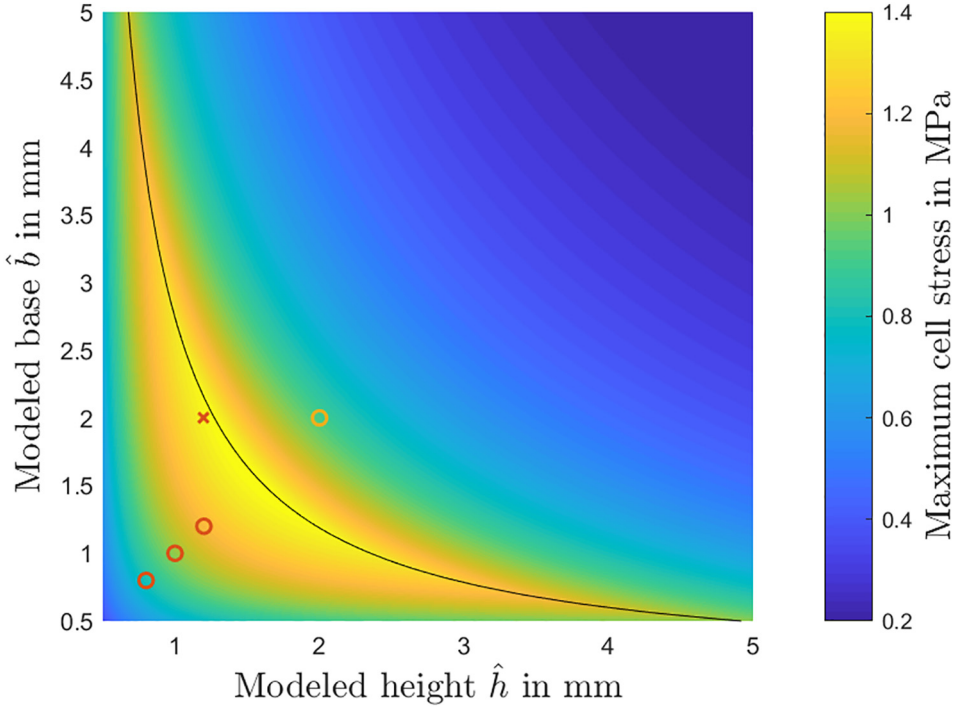

Fig. 4. Maximum cell stress plotted against cell parameters $\hat{b}$ and $\hat{h}$. The experimental samples are indicated with circles. A sample with a different length-to-base ratio (cross) was used to further verify the theoretical model.

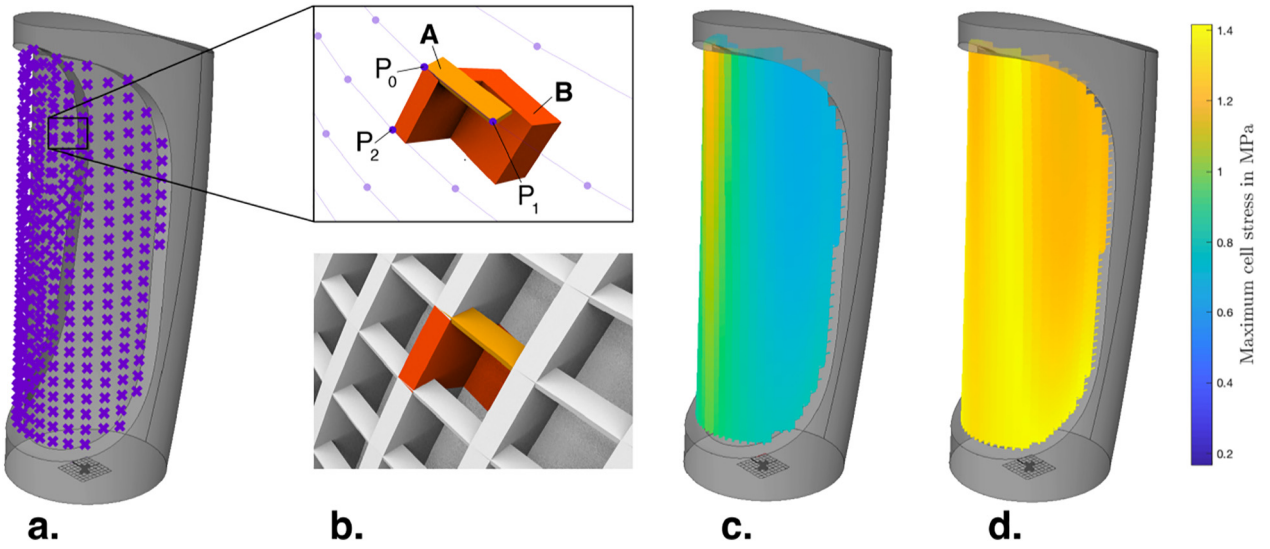

Fig. 5. Design automation. (a) Arrays of points applied to the double curved surface. (b) Placing, orienting, and scaling of parametric structure cell. (c) Generated structure with color visualization of $\sigma_{c_{max}}$ in first iteration (d) Final iteration with improved $\sigma_{c_{max}}$. (For interpretation of the references to color in this figure legend, the reader is referred to the Web version of this article.)

of the bonding. The model also assumes a uniform loading across all cells. In reality, the intensities and direction of the loads may vary across the cells.

2.3. Design automation

The structure cell can be linearly repeated to create an interlocking structure on a planar surface. However, applying the structure cell onto non-planar surfaces is less straightforward. Similar to quadrilateral meshing on double curved surfaces, a strategy for determining the shapes and sizes of the quadrilateral cells needs to be defined with the goal of matching the desired shape as closely as possible. In this case, the quadrilateral cell sizes and shapes need to be optimized according to their corresponding theoretical maximum stress $\sigma_{c_{max}}$ (indicated in Fig. 4) as well. At the same time, the printability of the structure needs to be guaranteed. This means that the crossover beams should be a continuous extrusion in the XY-plane of the printer, and the vertical beams need to satisfy the overhang constraints. To facilitate the generation of interlocking structures in such complex scenarios, an algorithmic process that automates the main part of the design for such structures was developed.

The algorithmic process was implemented in Grasshopper [26]. The first step in automation is the generation of a pattern of points on the surface (Fig. 5(a)). These points are used to position the structure cells. The pattern is built up of arrays of points that are located in XY-planes, meaning that the arrays are horizontal. The arrays are positioned as such that vertical alignment of successive arrays is maximized. The number of arrays and number of points in an array are provided by the designer.

A parametric structure cell is defined. The structure cell consists of two bodies, as illustrated in (Fig. 5(b)). Body A represents the crossover beam, while Body B represents the vertical beam and rear wall of the structure. The structure cell is repeatedly placed on the surface by coinciding the cell's origin with each point of the pattern. The length of Body A and Body B along the cell's x-axis are modified to match the euclidean distance between the current point P0 and the next point in the horizontal array P1. Then, rotating around origin P0, the x-axis of Body A is made collinear to the line between P0 and P1. This rotation is in the XY-plane, therefore Body A keeps its flat orientation. When completed

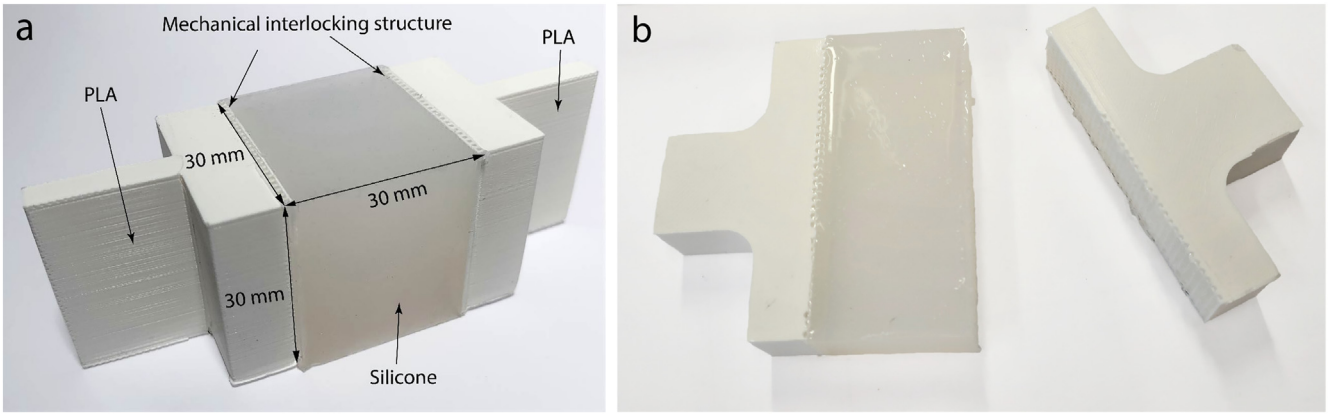

Fig. 6. (a) Dimensions of the tensile testing sample. (b) Sample with 4:1 width to height ratio after tensile testing.

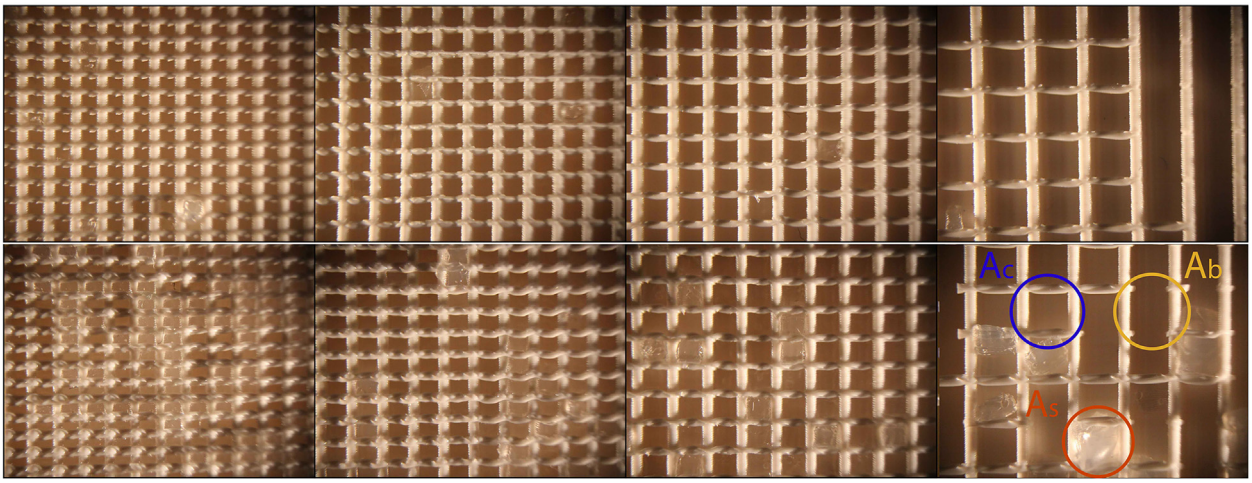

Fig. 7. Microscope pictures of interlocking structure after tensile testing. Top row: samples with 0.4 mm depth. Bottom row: samples with 0.8 mm depth. Circles indicate the specific failure mode of that cell.

for all points in the XY-plane, this operation generates a geometry that, after slicing, results in one continuously extruded crossover beam. The length of Body B along its z-axis is matched to the euclidean distance between P0 and P2, and its z-axis is made collinear to the line between P0 and P2. The end result is an interlocking structure that is conforming to the surface.

To provide feedback to the designer about the expected performance of the generated structure, the modeling described in section 2.2 is applied to calculate the $\sigma_{c_{max}}$ from the generated b and h for all cells. In the 3D preview (Fig. 5(c)), each cell is given the color corresponding to the $\sigma_{c_{max}}$ following the color scheme of Fig. 4. After evaluating the preview, the designer can choose to adjust the input settings for the point distribution, and obtain a structure with a more desirable $\sigma_{c_{max}}$ distribution (Fig. 5(d)). This way, knowledge on the load case of the product can be used to distribute the strength of the individual cells in a way that is optimal for the specific design.

The current automated design process has some limitations, which become more apparent when applied to less continuous geometries. Currently, the algorithm is developed for curved surfaces with small variations in curvature. Therefore, the solution for the point pattern does not require any iterative processes. For more complex and arbitrary geometries, the solution to generate a desired point pattern will not be trivial,

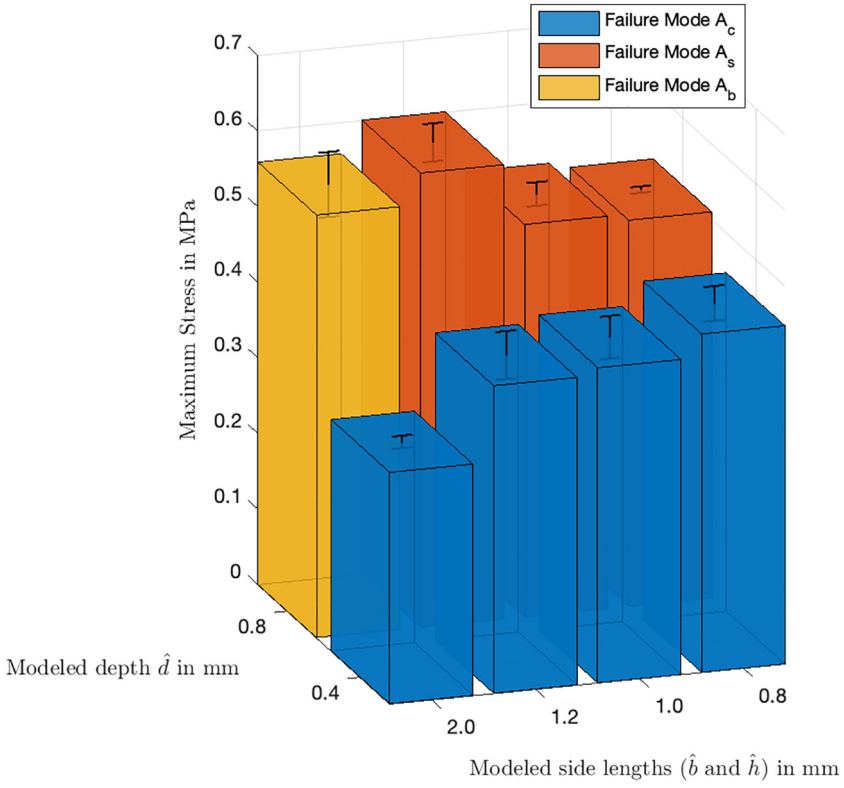

Fig. 8. Measured mean peak stress plotted against modeled depth $\hat{d}$ and modeled length of the sides ($\hat{b}$ and $\hat{h}$). The errorbars indicate the standard deviation. The color of the bar indicates the dominant failure mode. (For interpretation of the references to color in this figure legend, the reader is referred to the Web version of this article.)

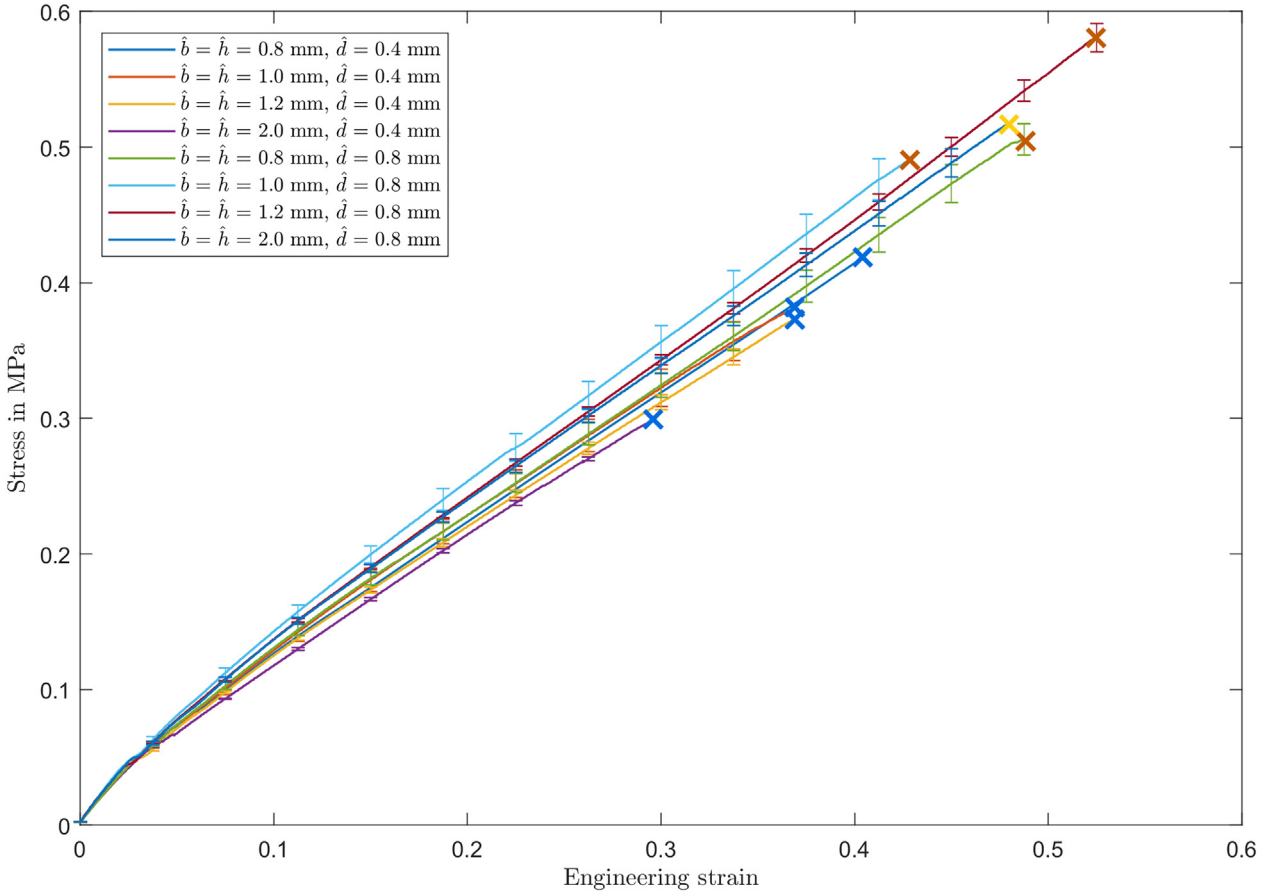

Fig. 9. Stress-strain curves for the different unit cell dimensions. The curves show the mean over the different samples. The error bars indicate the standard deviation. The maximum values of the curves indicate the highest stress of the weakest sample, as no useful mean can be obtained beyond this point. The colored crosses indicate the type of failure mode (matching the color coding of Fig. 8). (For interpretation of the references to color in this figure legend, the reader is referred to the Web version of this article.)

and other algorithms for pattern generation will need to be considered, such as the projection and relaxation strategy that was proposed by Reiner et al. [27]. Also, for surfaces with a small radius of curvature, the intended final structure cannot be guaranteed, since the overlap of neighboring structure cells becomes significant.

2.4. Experimental setup

Tensile tests were conducted to find the correspondence between the theoretical model from section 2.2 and the fabricated results. The design of the tensile test samples is illustrated in Fig. 6(a). The sample is composed of two hard elements with a silicone cube in between. The length, width and depth of the silicone part were determined at 30 mm. A bonding is realized through mechanical interlocking of the silicone around the 3D-printed structure on the hard parts. The strength of this bonding was evaluated by pulling the two hard parts apart until failure occurs. A series of three samples was fabricated for each of the experiments. All samples were tested on a *2014 Zwick* tensile testing machine. The tensile tests were performed at a speed of 5 mm/min, unless specified otherwise. The test was shut down once the force dropped to 80% of the maximum force measured. After tensile testing, the failure interface of the samples was studied using an *Olympus SZ61* microscope with directional lighting, and a DSLR camera was used to obtain the images.

2.4.1. Sampling strategy

The modeled depth ($\hat{d}$), height ($\hat{h}$) and base ($\hat{b}$) of the structure (as discussed in Section. 2.2) were varied throughout the experiments. The theoretical model shown in Fig. 4 was used as a guideline for the sampling strategy. Two additional samples series with changes in the parameters of the experimental setup were tested to investigate the influence of the sample dimensions and test speed on the results. Moreover, two series of samples without an interlocking structure were fabricated to benchmark the strength of the structure.

Modeled depth ($\hat{\mathbf{d}}$): The model assumes that no failure occurs in silicone surface A_c (see Fig. 3). Failure on A_c can be prevented by increasing the modeled depth $\hat{d}$. This results in an increased stiffness of the silicone body behind the crossover beams, preventing excessive deformation around the beams leading to failure.
As the goal was to minimize the depth for maximum applicability (see section 2.1), four series of samples with $\hat{h}$ and $\hat{b}$ at 0.8, 1.0 and 1.2 mm were first fabricated at a modeled depth $\hat{d}$ of 0.4 mm.From here on, new sample series with an increase in $\hat{d}$ in steps of 0.4 mm were fabricated and tested until a depth was found at which failure no longer occurred in surface A_c.

Modeled height ($\hat{\mathbf{h}}$) and base ($\hat{\mathbf{b}}$): After a depth was found at which the failure no longer occurs at surface A_c, the samples with $\hat{h}$ and $\hat{b}$ of 0.8, 1.0, 1.2 and 2.0 mm were used to find the correspondence with the theoretical model. Although the samples with $\hat{h}$ and $\hat{b}$ at 0.8, 1.0 and 1.2 mm (indicated with red circles in Fig. 4) are relatively close to each other in dimensions, the theoretical model predicts a large change in maximum cell stress over these samples. Therefore,

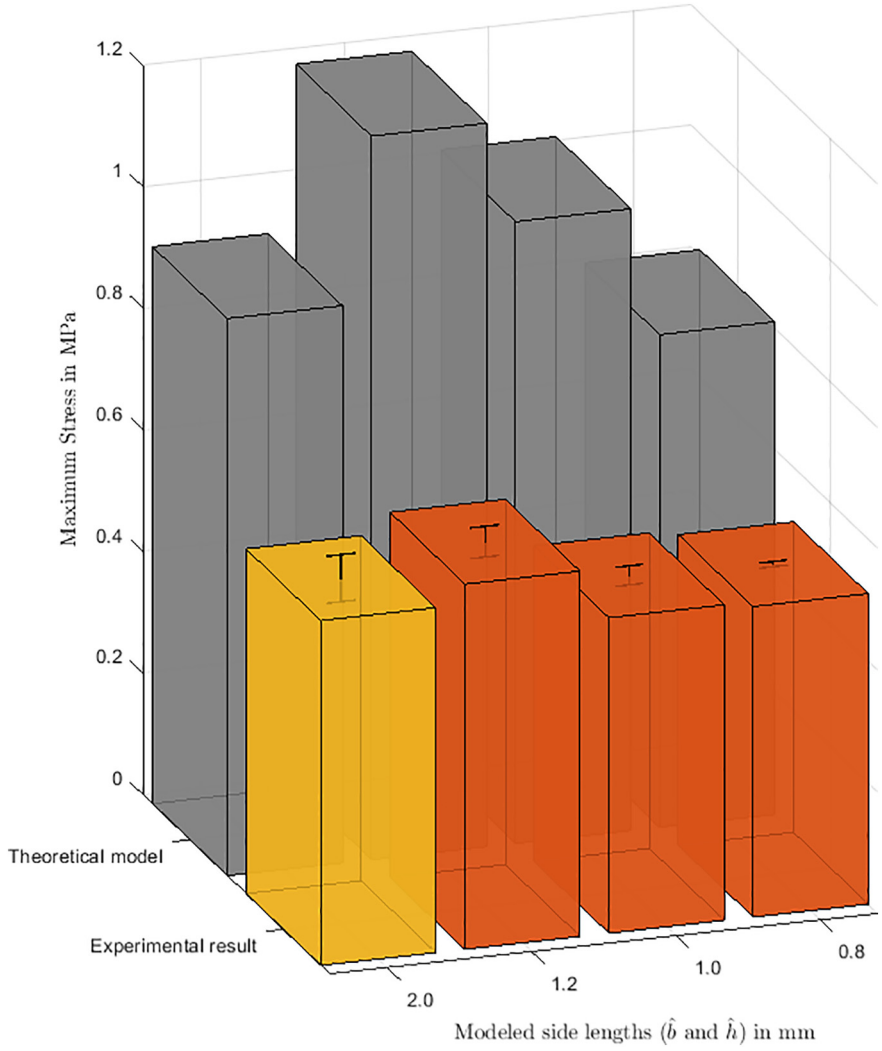

Fig. 10. Comparison of the mean peak stresses of the theoretical model with the experimental results for $\hat{d} = 0.8$ mm.

these samples were used to identify where this steep change occurs in the experimental results. The sample series with $\hat{h}$ and $\hat{b}$ at 2.0 mm (indicated with a yellow circle in Fig. 4) is on the right side of the black line. Therefore, it was expected to fail due to shear stress in the beams instead of failure in the silicone surface A_s. To verify how well the experimental results match the model for deviating $\hat{h}$: $\hat{b}$ ratios, a sample series with $\hat{h} = 1.2$ mm and $\hat{b} = 2$ mm was fabricated (indicated with the red cross in Fig. 4). Although its ratio is less optimal, this series was expected to outperform the other samples in maximum cell stress. Moreover, as this series is close to the black line where $F_{c,b_{max}} = F_{c,s_{max}}$, both failure modes could be expected to occur here.

Experimental setup parameters: Two series of samples with deviating dimensions were fabricated to investigate the influence of 'necking' (a decrease in local cross sectional area upon stretching), change in the force direction due to necking, and tensile testing speed on the results. The necking effect was investigated through a sample series with a width to height ratio of 4 : 1, but equal cross-sectional area (see Fig. 6(b)). An additional sample series with a regular width to height ratio was tested at a higher speed of 50 mm/min respectively. These tests were performed with the cell parameters $\hat{h}$ and $\hat{b}$ chosen at 1.2 mm and the minimum depth $\hat{d}$ for which failure did not occur at surface A_c.

Benchmark samples: Two series of samples without the mechanical interlocking structure were prepared in order to benchmark the bonding strength of the interlocking structure. The first series of samples without bonding structure did not have any additional bonding technique, whereas the second series used a coating of a commercially available primer (*Smooth-on Sil-Poxy*) at the contact interfaces to increase the bonding between the thermoplastic parts and the silicone.

2.4.2. Materials and fabrication

The hard parts of the samples were printed on an Ultimaker 2 + using FDM technology. The unit cells were generated starting from the edges of the two bonding interfaces. Therefore, uncompleted cells occur at the opposing edges of the sample whenever the length and width of the sample is not an exact multiple of the cell size. The percentage of area that contains uncompleted cellsranges from 0.67 % (for $\hat{h}$ and $\hat{b} = 1.0$ mm) to 5.3 % (for $\hat{h}$ and $\hat{b} = 2.0$ mm). White PLA and standard settings were used (slicing software used is Cura 3) for all samples. Standard settings are 0.1 mm layer height and a 0.4 mm nozzle. The material has a yield strength of 49.5 MPa and an elongation at yield of 3.3 % [28].

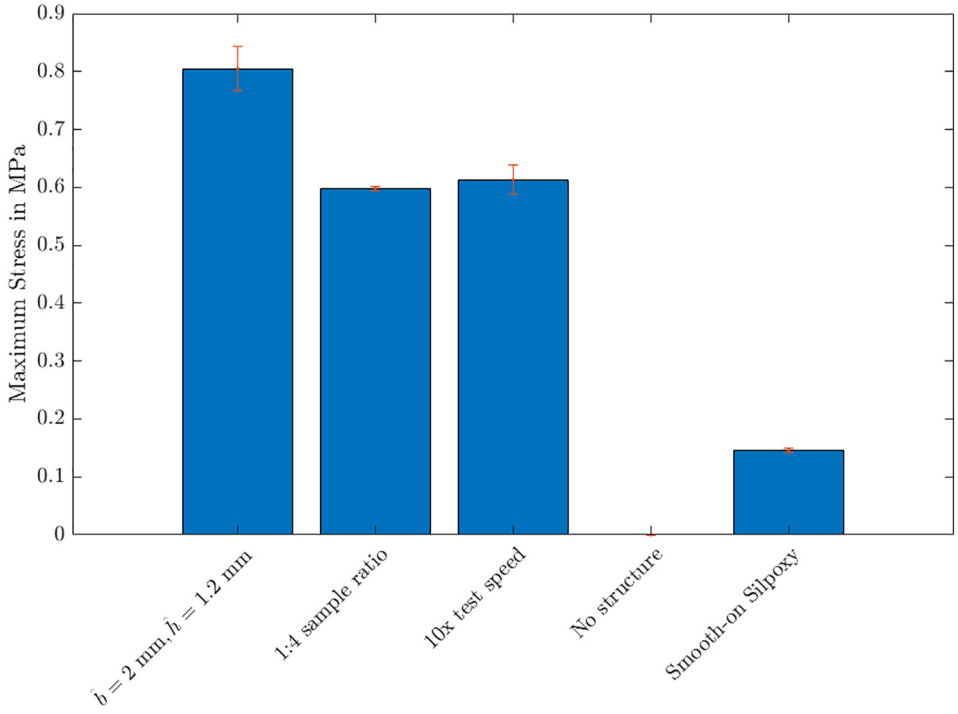

Fig. 11. From left to right: (a) Mean peak stress of the sample series with $\hat{b}$ of 2 mm and a $\hat{h}$ of 1.2 mm. (b) Mean peak stress of the sample series with a 1 : 4 width to height ratio. (c) Mean peak stress of the sample series tested at a speed of 50 mm/min. (d) Mean peak stress of the benchmark sample series without primer. (e) Mean peak stress of the benchmark sample series with primer. The errorbars indicate the standard deviation. The benchmark samples with no structure fell apart before a force could be measured.

Reusable molds with a negative shape of the desired test sample were printed as well. Two hard parts were placed inside this mold, after which the silicone was poured into the remaining void. Two component addition curing RTV silicone with shore hardness A40 [29] was used for all samples. The yield strength of the silicone was determined at 2.5 MPa. The silicones were manually mixed, as prescribed, in a mass ratio of 1 to 10 and placed inside a vacuum for 7 min to decrease the amount of air pockets. The silicone was allowed to cure for 24 h at room temperature before testing.

3. Results

First, this section will discuss the results of the experiments described in section 2.4. Hereafter, several applications of the 3D-printed mechanical interlocking structure will be demonstrated, making use of the modeling technique described in section 2.2.

3.1. Mechanical interlocking structure

Modeled depth ($\hat{\mathbf{d}}$): At a depth $\hat{d}$ of 0.4 mm, the dominant failure mode occurred at surface A_c. This failure mode allows the silicone to be 'pulled out' of the hard part, leaving empty cells with intact beams as indicated with the blue circle in Fig. 7. At this depth, the maximum stress decreases with an increasing $\hat{b}$ and $\hat{h}$, as can be seen in Fig. 8. This can be explained by the reduced surface area of the crossover beams, causing the beams to generate higher stresses on the silicone body behind the beams at equal forces. At a depth $\hat{d}$ of 0.8 mm, the dominant failure no longer occurs at surface A_c. Instead, a failure of the beam or silicone surface A_s is observed, indicated with a yellow and red circle in Fig. 7 respectively. A failure at surface A_s can be recognized by intact beams with pieces of silicone remaining underneath the interlocking structure, whereas a failure at the crossover beams can be recognized by missing crossover beams. As the silicone is more firmly held into the structure, the samples with $\hat{d} = 0.8$ also have a higher stiffness, as can be observed in Fig. 9.

Modeled height ($\hat{\mathbf{h}}$) and base ($\hat{\mathbf{b}}$): Fig. 8 shows the mean peak stresses of the cells for which $\hat{b} = \hat{h}$ at a $\hat{d}$ of 0.8. It can be seen that these stresses are much higher than the ones at a $\hat{d}$ of 0.4, with the highest stress measured for the sample with a $\hat{b}$ and $\hat{h}$ of 1.2 mm. The trade-off between the two failure modes seems to occur between 1.2 mm and 2.0 mm. This is in good agreement with the theoretical model, as is illustrated in Fig. 10. Although the trends and optimal parameters agree well with the model, the magnitudes of the measured peak stresses are significantly lower than the theoretical results. A mean peak stress of 0.6 MPa was measured for the 1.2 mm samples, as compared to a 1.2 MPa stress predicted by the theoretical model. This can be due to several factors such as inconsistent beam thickness, micro air bubbles in the silicone and consecutive cell failure. A brief zipping sound could be heard during failure, indicating that the cells do not fail at the exact same time. The sample series with a $\hat{b}$ of 2 mm and a $\hat{h}$ of 1.2 mm, was expected to outperform the other samples in terms of maximum stress. The experimental results confirm this with a mean maximum stress of 0.805 MPa (Fig. 11) as compared to a mean maximum stress of 0.601 MPa for the samples with a $\hat{b}$ and $\hat{h}$ of 1.2 mm.

Experimental setup parameters: The results of these sample series are shown in Fig. 11. The sample series with a 1 : 4 width to height ratio (Fig. 6(b)) shows that there is some loss in strength due to increased necking, with a mean peak stress of 0.573 MPa as compared to a mean peak stress of 0.601 MPa for the sample with a width and height of 30 mm. The sample series that was tested at a higher speed of 50 mm/min resulted in a slightly higher peak strength (0.620 MPa), because the viscous component of the viscoelastic silicone gives a strain rate dependent on time. High speed loads are likely to occur in the soft robotics application described below, where air chambers are inflated rapidly.

Benchmark samples: The adhesion strength of the silicone to a flat plastic surface without bonding structure was so low that the samples would separate when clamping them into the testing machine. Using *Smooth-on Sil-Poxy* as a primer resulted in an average maximum stress of 0.146 MPa, as shown in Fig. 11, which is more than five times lower than the 0.805 MPa that was obtained using the mechanical interlocking structure with a $\hat{b}$ of 2 mm and an $\hat{h}$ of 1.2 mm.

3.2. Applications

Three different application directions of the presented design and fabrication approach are demonstrated. These examples show how prototyping and manufacturing of end-use custom parts can be realized. The fabrication steps are identical to those in Fig. 1. Injection points and flow channels for the silicone are designed for each specific part.

3.2.1. Over molded parts

A customized bike handle was fabricated with the presented method (Fig. 12(a and b)). The starting shape was a free-form handle design. This shape was subdivided into a hard plastic core and a silicone skin. In this example, the skin has a uniform thickness. Using the design automation tool discussed in section 2.3, the point sampling density was iteratively chosen, and the interlocking structure was generated.

Over molding can also be applied on 3D printed soft robotics. Fig. 12(c and d) illustrate how the grip of an originally mono-material soft robotic finger [30] can be improved through an over molded silicone finger tip which also creates a food safe contact surface. This specific silicone finger tip has a gecko-inspired contact surface to illustrate the ability of applying custom elements to increase functionality. Moreover, this demonstrates the

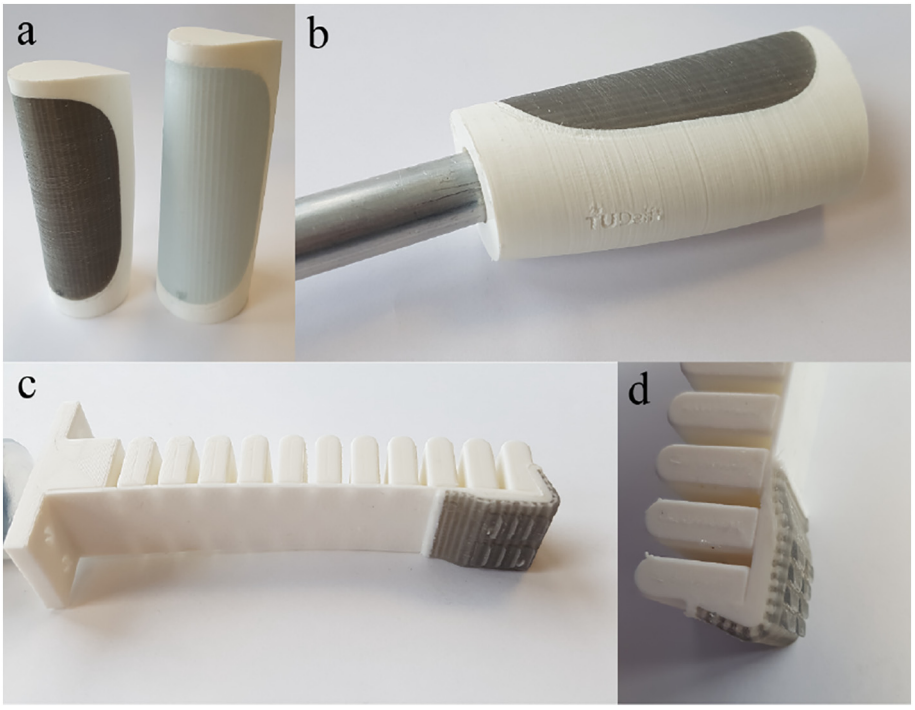

Fig. 12. Examples of over molded parts fabricated using the presented method. (a) Custom handles. (b) Handle in context. (c) Soft robotic finger with over molded silicone finger tip. (d) Close-up of silicone gripping element.

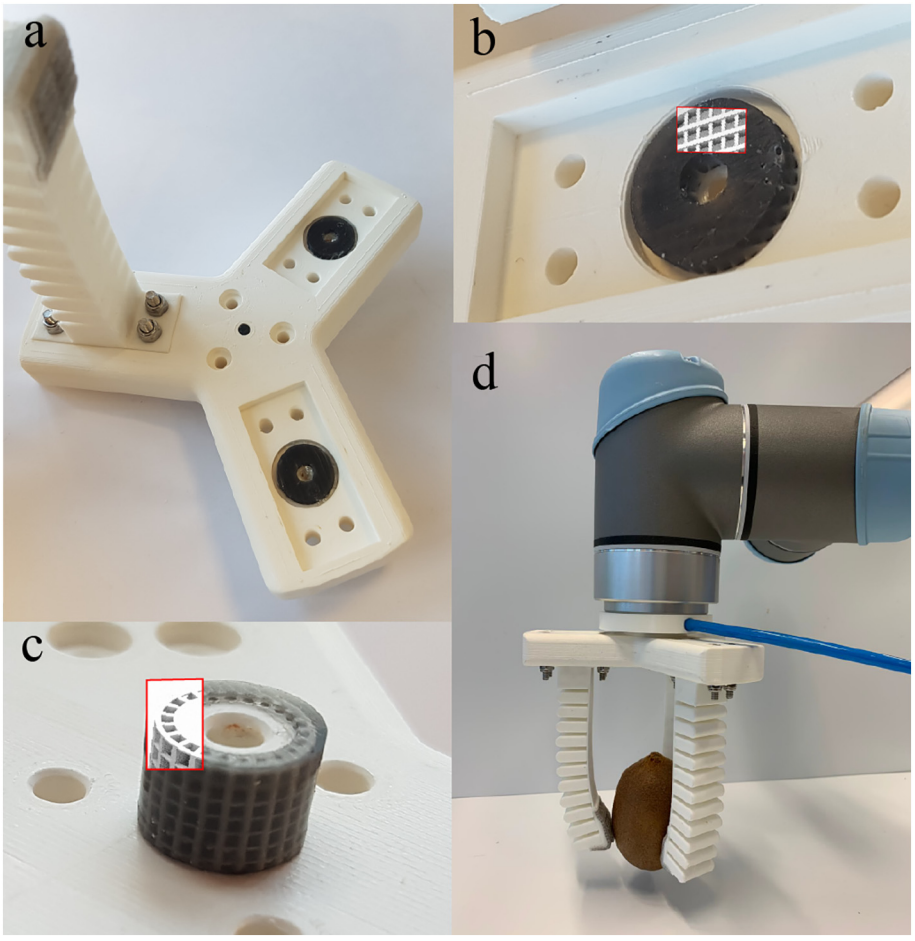

Fig. 13. Integrated seals fabricated using the presented method. (a) Base station with one assembled finger. (b) Gasket, the red outlined area shows the structure in CAD. (c) Barb, the red outlined area shows the structure in CAD. (d) Assembly of base station and fingers on a robotic arm grasping a kiwifruit. (For interpretation of the references to color in this figure legend, the reader is referred to the Web version of this article.)

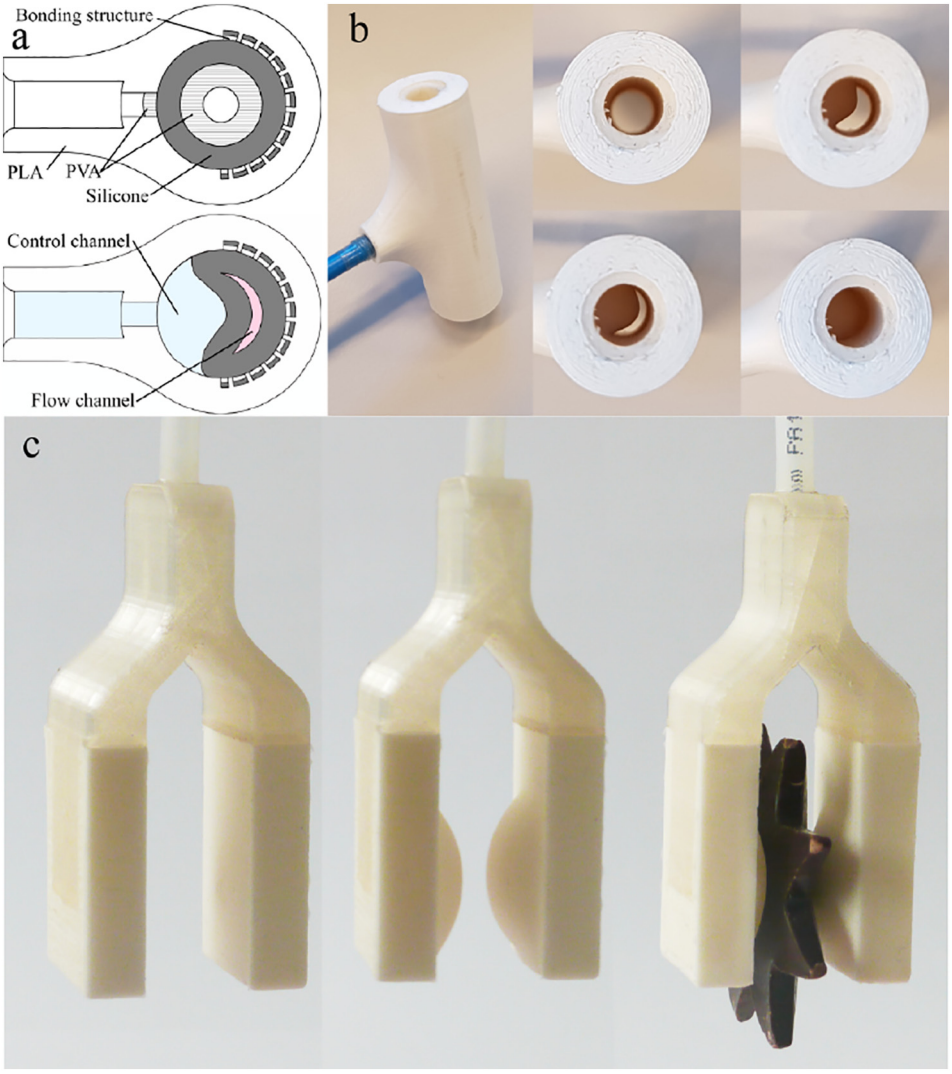

Fig. 14. Soft pneumatic actuators fabricated by selectively applying the mechanical interlocking structure. (a) Schematic cross section (striped sections indicate PVA material and dark sections indicate silicone material). (b) Pneumatic organic valve. (c) Pneumatic gripper.

freedom of combining different types of 3D printing plastics, like TPU, with silicone material.

3.2.2. Integrated seals

The presented design and fabrication approach can also be used to manufacture soft integrated seals. As an example part, a base station for the soft robotic fingers was fabricated (Fig. 13(a)). This part has integrated silicone gaskets to make an airtight connection with the soft robotic fingers (Fig. 13(b)) and a silicone barb to make an airtight connection with the base of the robot arm (Fig. 13(c)). The functioning assembly on a robot arm is illustrated in Fig. 13(d) gripping a kiwifruit.

3.2.3. Multi-material soft pneumatic actuators

The application of the presented approach to fabricate compact multi-material soft pneumatic actuators is also presented. Here, the structure is selectively applied on those areas of the surface where the silicone and plastic are intended to create an airtight bond (i.e. the edges of the air chamber), Fig. 14(a). The areas that are intended to inflate are intentionally left blank. Once the silicone is cast on top of the entire surface, a zero-thickness air chamber is created that can be inflated through air channels that are embedded in the plastic part. Fig. 14(b) shows a pneumatically actuated air valve. It works similar to a Quake-style microvalve [31] but on a larger scale. The normally open valve can control the flow rate by inflating the air chamber on the inside of the valve. Fig. 14(c) shows a soft robotic gripper with two zero-thickness air chambers inflated through air channels that are embedded in the plastic part. The gripper can be used to grasp fragile objects.The application of the presented approach to fabricate compact multi-material soft pneumatic actuators is also presented. Here, the structure is selectively applied on those areas of the surface where the silicone and plastic are intended to create an airtight bond (i.e. the edges of the air chamber), Fig. 14(a). The areas that are intended to inflate are intentionally left blank. Once the silicone is cast on top of the entire surface, a zero-thickness air chamber is created that can be inflated through air channels that are embedded in the plastic part (Fig. 14(b). Fig. 14(c) shows a soft robotic gripper with two zero-thickness air chambers inflated through air channels that are embedded in the plastic part. The gripper can be used to grasp fragile objects.

4. Conclusion

A method to control the bonding between silicone and plastic parts through mechanical interlocking was presented. The method makes use of a hybrid fabrication process where silicone is cast over a 3D-printed structure. The influence of the design parameters of the structure on the bonding strength was demonstrated both theoretically and experimentally. Using a cell with a modeled height and base of 1.2 mm, a bonding strength of over 0.805 MPa was achieved (taking in mind the yield strength of the silicone (2.5 MPa) and plastic (49 MPa)) as compared to a bonding strength of 0.146 MPa using a specialized commercially available adhesive.

A CAD tool was developed to apply the interlocking structure to free-form shapes in an automatic way and with a minimal influence on the design freedom. Fabricated parts demonstrate the ability to locally control the bonding, which can be used for novel designs in the field of soft robotics.

The authors expect that an even higher bonding strength could be realized through further optimization of the fabrication process, material selection, and structure design.

Furthermore, with the rise of Multi-Material Additive Manufacturing there will be challenges in recycling and separating the individual materials. The presented approach is promising because there is no chemical bonding. Future research might focus on optimising the structure for disassembly.

Declaration of interests

The authors declare that they have no known competing financial interests or personal relationships that could have appeared to influence the work reported in this paper.

CRediT authorship contribution statement

Lars Rossing: Conceptualization, Data curation, Formal analysis, Writing - original draft, Writing - review & editing. **Rob B.N. Scharff:** Conceptualization, Formal analysis, Writing - original draft, Writing - review & editing. **Bryan Chömpff:** Conceptualization, Data curation, Formal analysis, Writing - review & editing. **Charlie C.L. Wang:** Conceptualization, Writing - original draft, Writing - review & editing. **Eugeni L. Doubrovski:** Conceptualization, Formal analysis, Writing - original draft, Writing - review & editing.

Appendix A. Supplementary data

Supplementary data to this article can be found online at https://doi.org/10.1016/j.matdes.2019.108254.

References

[1] V. Seitz, K. Arzt, S. Mahnel, C. Rapp, S. Schwaminger, M. Hoffstetter, E. Wintermantel, Improvement of adhesion strength of self-adhesive silicone rubber on thermoplastic substrates – comparison of an atmospheric pressure plasma jet (appj) and a pyrosil® flame, Int. J. Adhesion Adhes. 66 (2016) 65–72.
[2] Hans-Heinrich Moretto, Manfred Schulze, Gebhard Wagner, Silicones, Ullmann's Encyclopedia of Industrial Chemistry (2000).
[3] Daniela Rus, Michael Tolley, Design, fabrication and control of soft robots, Nature 521 (2015) 467–475.
[4] Bobak Mosadegh, Panagiotis Polygerinos, Christoph Keplinger, Sophia Wennstedt, Robert F. Shepherd, Unmukt Gupta, Jongmin Shim, Katia Bertoldi, Conor J. Walsh, George M. Whitesides, Pneumatic networks for soft robotics that actuate rapidly, Adv. Funct. Mater. 24 (15) (2014) 2163–2170.
[5] Regina M. Gouker, Satyandra K. Gupta, Hugh A. Bruck, Holzschuh Tobias, Manufacturing of multi-material compliant mechanisms using multi-material molding, Int. J. Adv. Manuf. Technol. 30 (11) (2006) 1049–1075.
[6] Andrew T. Gaynor, Nicholas Alexander Meisel, Christopher B. Williams, James K. Guest, Multiple-material topology optimization of compliant mechanisms created via polyjet three-dimensional printing, J. Manuf. Sci. Eng. Trans. ASME 136 (6) (2014) 12.
[7] Ashis Gopal Banerjee, Xuejun Li, Greg Fowler, Satyandra K. Gupta, Incorporating manufacturability considerations during design of injection molded multi-material objects, Res. Eng. Des. 17 (4) (Mar 2007) 207–231.
[8] A. Baldan, Adhesion phenomena in bonded joints, Int. J. Adhesion Adhes. 38 (2012) 95–116.
[9] Multicomponent polymeric materials, John Wiley & Sons, Ltd, 2005 687–756 Chapter 13.
[10] R. Ma Raymond, Joseph T. Belter, Aaron M. Dollar, Hybrid deposition manufacturing: design strategies for multimaterial mechanisms via three-dimensional printing and material deposition, J. Mech. Robot. 7 (05 2015), 021002.
[11] Firas Awaja, Michael Gilbert, Georgina Kelly, Bronwyn Fox, Paul J. Pigram, Adhesion of polymers, Prog. Polym. Sci. 34 (9) (2009) 948–968.
[12] Tsung-Chan Tsai, Jeffrey S. Louis, Sameer Kalghatgi, Daphne Pappas Antonakas, Robert L. GCy, Shirley Zhu abd, Kirill Gutsol, Xinpei Lu, 3d printers having plasma applicators and methods of using same, 2016 Patent No. US20160271874A1, Filed 2016 March 21st.
[13] Z. Fang, J. Yang, Y. Liu, T. Shao, C. Zhang, Surface treatment of polyethylene terephthalate to improving hydrophilicity using atmospheric pressure plasma jet, IEEE Trans. Plasma Sci. 41 (6) (June 2013) 1627–1634.
[14] Osman Dogan YirmibesogluJohn Morrow, Stephanie Walker, Gosrich Walker, Reece Aidan Canizares, Hansung Kim, Uranbileg Daalkhaijav, Chloe Fleming, Callie Branyan, Yigit Meng, Direct 3d printing of silicone elastomer soft robots and their performance comparison with molded counterparts, IEEE-RAS International Conference on Soft Robotics. , ROBOSOFT), 2018.
[15] Farzad Liravi, Ehsan Toyserkani, Additive manufacturing of silicone structures: a review and prospective, Addit. Manuf. 24 (2018) 232–242.
[16] Nicholas W. Bartlett, Michael T. Tolley, T. Johannes, B. Overvelde, James C. Weaver, Bobak Mosadegh, Katia Bertoldi, George M. Whitesides, Robert J. Wood, A 3d-printed, functionally graded soft robot powered by combustion, Science 349 (6244) (2015) 161–165.
[17] Eric MacDonald, Wicker Ryan, Multiprocess 3d printing for increasing component functionality, Science 353 (6307) (2016).
[18] L. Rossing, Ulticast: Designing an Add-On that Creates New Material Benefits and Increases the Printing Speed for FDM Printed Parts, TUDelft Repository, 2016.
[19] John Ryan C. Dizon, Alejandro H. Espera, Qiyi Chen, Rigoberto C. Advincula, Mechanical characterization of 3d-printed polymers, Addit. Manuf. 20 (2018) 44–67.
[20] F. M. da Silva Lucas, Ricardo J.C. Carbas, Mariana D. Banea, Failure Strength Tests, Springer International Publishing, Cham, 2018 489–521.
[21] A. Khudiakova, F. Arbeiter, M. Spoerk, M. Wolfahrt, D. Godec, G. Pinter, Inter-layer bonding characterisation between materials with different degrees of stiffness processed by fused filament fabrication, Addit. Manuf. 28 (2019) 184–193.
[22] Ivan Q. Vu, Lindsey B. Bass, Christopher B. Williams, David A. Dillard, Characterizing the effect of print orientation on interface integrity of multi-material jetting additive manufacturing, Addit. Manuf. 22 (2018) 447–461.
[23] Thomas S. Lumpe, Jochen Mueller, Kristina Shea, Tensile properties of multi-material interfaces in 3d printed parts, Mater. Des. 162 (1 – 9) (2019).
[24] ASTM International, Standard Test Method for Tensile Properties of Plastics D638-14. 01, 2004.
[25] Jérémie Dumas, Hergel Jean, Sylvain Lefebvre, Bridging the gap: automated steady scaffoldings for 3d printing, ACM Trans. Graph. 33 (4) (2014) 98.
[26] Davidson Scott, Grasshopper - Algorithmic Modeling for Rhino, 2019.
[27] Tim Reiner, Nathan Carr, Radomír Měch, Ondřej Šťava, Carsten Dachsbacher, Gavin Miller, Dual-color mixing for fused deposition modeling printers, Comput. Graph. Forum 33 (2) (2014) 479–486.
[28] Ultimaker PLA. Accessed: 2018–12–15
[29] Silicones and more A40, 2018 12–15 Accessed.
[30] R.B.N. Scharff, J. Wu, J.M.P. Geraedts, C.C.L. Wang, Reducing out-of-plane deformation of soft robotic actuators for stable grasping, 2019 2nd IEEE International Conference on Soft Robotics (RoboSoft) April 2019, pp. 265–270.
[31] Marc A. Unger, Hou-Pu Chou, Thorsen Todd, Axel Scherer, Stephen R. Quake, Monolithic microfabricated valves and pumps by multilayer soft lithography, Science 288 (5463) (2000) 113–116.